



HAL
open science

Angle-resolved studies of XUV–IR two-photon ionization in the RABBITT scheme

J Joseph, F Holzmeier, D Bresteau, C Spezzani, T Ruchon, J Hergott, O Tcherbakoff, P D'oliveira, J Houver, D Doweck

► **To cite this version:**

J Joseph, F Holzmeier, D Bresteau, C Spezzani, T Ruchon, et al.. Angle-resolved studies of XUV–IR two-photon ionization in the RABBITT scheme. *Journal of Physics B: Atomic, Molecular and Optical Physics*, 2020, 53 (18), pp.184007. 10.1088/1361-6455/ab9f0d . hal-04459186

HAL Id: hal-04459186

<https://hal.science/hal-04459186v1>

Submitted on 15 Feb 2024

HAL is a multi-disciplinary open access archive for the deposit and dissemination of scientific research documents, whether they are published or not. The documents may come from teaching and research institutions in France or abroad, or from public or private research centers.

L'archive ouverte pluridisciplinaire **HAL**, est destinée au dépôt et à la diffusion de documents scientifiques de niveau recherche, publiés ou non, émanant des établissements d'enseignement et de recherche français ou étrangers, des laboratoires publics ou privés.

Angle-resolved studies of XUV-IR two-photon ionization in the RABBITT scheme

J Joseph¹, F Holzmeier^{1,2}, D Breteau³, C Spezzani^{3,4,5}, T Ruchon³, J F Hergott³,
O Tcherbakoff³, P. D'Oliveira³, J C Houver¹ and D Dowek¹

¹Université Paris-Saclay, CNRS, Institut des Sciences Moléculaires d'Orsay, 91405, Orsay, France

²Université Paris-Saclay, Synchrotron Soleil, 91190, Saint-Aubin, France

³Université Paris-Saclay, CEA, CNRS, LIDYL, 91191, Gif-sur-Yvette, France

⁴Université Paris-Saclay, CNRS, Laboratoire de Physique des Solides, 91405, Orsay, France

⁵Eletra-Sincrotrone, Trieste, Basovizza, 34149, Italy

E-mail: jennifer.joseph@universite-paris-saclay.fr, danielle.dowek@u-psud.fr

Received xxxxxx

Accepted for publication xxxxxx

Published xxxxxx

Abstract

Reconstruction of attosecond beating by interference of two-photon transitions (RABBITT) is an established technique for studying time-delay in photoionization of atoms and molecules. It has been recently extended to angle-resolved studies, accessing diverse fingerprint observables of the attosecond photoemission dynamics within the bound-continuum and continuum-continuum transitions. In this work, we address the general form of the $I_{SB}(\theta, \tau)$ two-photon photoelectron angular distributions (PADs) associated to the RABBITT sideband signal, as a function of the emission angle θ , and the delay τ between the XUV attosecond pulse train and the infrared (IR) dressing field at play in the RABBITT scheme. Relying on the expansion in Legendre polynomials, the PAD is synthesized in terms of a reduced set of coefficients which fully describe both its static (τ -independent) and dynamic (τ -dependent) components and enables us to retrieve any observable characterizing the PAD. This unified framework streamlines the comparison between different experimental or theoretical data sets and emphasizes how some observables depend on the experimental conditions. Along with the modelled analysis, we report new results of angle-resolved RABBITT direct ionization of the np valence orbital of Ar($3p^6$) and Ne($2p^6$), employing electron-ion coincidence momentum spectroscopy at the new Attolab facility. In this case, the nine coefficients synthesizing the PAD are further linked to the magnitude and phase of the transition dipole matrix elements, providing a fundamental test of theoretical predictions. Similarities and differences are found between Ar and Ne in the explored low energy region, up to 20 eV above the ionization threshold, where the electron dynamics is most sensitive to electronic correlation. Further interpretation of these results would benefit from a comparison with advanced many-body theoretical simulations.

Keywords: RABBITT, photoionization, atoms, photoelectron angular distribution, atomic delay

1. Introduction

Interferences between two quantum paths involving identical initial and final electronic states of atoms or

molecules have motivated a number of two-color photoionization studies. Extending earlier investigations using coherent optical laser fields [1], most recent studies take advantage of the development of advanced sources of XUV

light pulses such as laser based high-order harmonic generation (HHG) [2] or free electron lasers (FEL) [3]. In such experiments, recording the variation of observables, like the ionization yield or the photoelectron angular distribution, with the relative phase of the light fields, gives access to complex transition matrix elements i.e., to dynamical parameters of the transition.

In the XUV-IR RABBITT (Reconstruction of attosecond beating by interference of two-photon transitions) two-photon scheme [2,4,5], an attosecond XUV pulse train (APT) consisting of a comb of odd high-order harmonics (HH) of a fundamental angular frequency ω ionizes a gas target in the presence of an additional phase-locked weak IR field of frequency ω , which induces continuum to continuum transitions. Therefore, a sideband (SB) of order $2q$ is produced in the photoelectron spectra (PES) at an intermediate electron kinetic energy (E_e), in between the peaks assigned to direct ionization by the harmonics HH_{2q-1} and HH_{2q+1} , by absorption or stimulated emission of one IR photon, respectively. These two pathways resulting in the same final state lead to interference between the XUV \pm IR two-photon scattering amplitudes. The 2ω modulation of the SB_{2q} yield as a function of the time delay τ , characterizing the phase-shift between the APT field and the optical field ω [2,6], constitutes the $I_{\text{SB}}(\tau)$ RABBITT observable, represented as:

$$I_{\text{SB}}(\tau) = A + B \cos(2\omega\tau + \Delta\phi). \quad (1)$$

Initially applied for the characterization of the harmonic phases forming an APT [2,7,8], the RABBITT scheme has been extended to investigate photoionization (PI) dynamics in real time at the atto-to-femtosecond scale. Indeed, the phase shift $\Delta\phi = \Delta\phi_{\text{XUV}} + \Delta\phi_{\text{A}}$ includes both the attochirp ($\Delta\phi_{\text{XUV}} = \phi_{2q+1} - \phi_{2q-1}$) describing the group delay of the attosecond pulse, and an intrinsic atomic phase $\Delta\phi_{\text{A}}$ which results from the two-photon transition defining the atomic time delay $\tau_{\text{A}} = \Delta\phi_{\text{A}}/2\omega$ (or more generally $\tau_{\text{T}} = \Delta\phi_{\text{T}}/2\omega$ for an atomic or a molecular target). The latter combines the Wigner time delay [9] of the PE wavepacket generated in the one-XUV photon bound-to-continuum (bc) ionization and that associated with the continuum-continuum (cc) transition, averaged over the θ emission angle, $\tau_{\text{T}} = \tau_{\text{W}} + \tau_{\text{cc}}$ [6,10–13]. Probing ultrafast electron dynamics in RABBITT experiments was demonstrated by measuring atomic phase or time delay differences between e.g., ionization from distinct subshells or sublevels of a single atomic [10,14–16] or molecular target [17,18], or from the outer shells of several atoms [19,20], or between electrons emitted in opposite directions from asymmetric molecular targets [21]. Thereby temporal signatures of electronic processes such as Cooper minima [14], autoionizing states or shape resonances in the ionization continuum of atoms [22–24] and molecules [17,18] or electron localization [21] were obtained.

The first angle-resolved experiments of XUV-IR two-photon ionization of atoms based on the superposition of an APT and a phase-locked dressing IR laser, measured using velocity map imaging (VMI) [25], demonstrated that the relative phase of the harmonics composing the APT is also encoded in the photoelectron angular distribution (PAD) of the SB signal, $I_{\text{SB}}(\theta, \tau)$, where θ is the polar emission angle relative to the linear polarization axis \mathbf{P} , common to the XUV and IR fields. Subsequent XUV-IR PI angle-resolved studies aimed for extracting information on the two-photon ionization dynamics in experiments of increasing temporal resolution, involving τ delays averaged on the few fs scale in two-color two-photon above threshold ionization (ATI) [26,27], specific attosecond controlled delays [28], then temporal resolution in the RABBITT scheme [29–33].

Most recent studies, based on electron-ion momentum coincidence spectroscopy or VMI, address in particular the interpretation of the angular dependence of the τ_{A} atomic time delays, arising from the τ_{W} and/or τ_{cc} contributions to the two-photon ionization dynamics. Consistent with angle-integrated RABBITT studies, the general form of $I_{\text{SB}}(\theta, \tau)$ was expanded as:

$$I_{\text{SB}}(\theta, \tau) = A(\theta) + B(\theta) \cos(2\omega\tau + C(\theta)), \quad (2)$$

where the observables can be extracted from a cosine fit of the delay-dependent SB signal for successive angular sectors corresponding to a θ polar angle emission direction [29,31,34]. Accordingly, the term $C(\theta)$ includes the phases associated with both one photon ionization and continuum-continuum coupling as a function of the emission angle.

Scrutinizing the one and two-photon steps, with the major goal to probe Wigner time delays characterizing the single-XUV photon ionization dynamics, strongly relies on the theoretical modelling of the RABBITT scheme extended to account for the angular distributions, based on second-order perturbation theory [11,35,36], time-dependent Schrödinger equation (TDSE) [34,37–39], or soft photon approximation (SPA) [40]. Additional refinements in the theoretical modelling relying on the random phase approximation with exchange (RPAE) [41–44], multiconfiguration Hartree-Fock (MCHF) [45] methods, or time dependent R matrix [46,47] include interchannel coupling, and correlation effects. Benchmarking such theoretical advances motivates the development of most complete PI experiments in atoms and molecules, angularly and temporally resolved at the attosecond time scale.

In this work, the main scope is to promote a unified formalism which allows to synthesize the $I_{\text{SB}}(\theta, \tau)$ RABBITT PADs by a reduced set of coefficients. This development, relying on the explicit expansion of the PAD in Legendre polynomials [25,48,49], enables us to retrieve any observable characterizing the PAD and provides an efficient mean to compare systematically an ensemble of experimental and theoretical results. This set of coefficients is expressed in

terms of the complex dipole matrix elements of the PI process, thereby it enables us as well to discuss the completeness of the performed angle-resolved RABBITT experiment.

This method is illustrated by recent measurements of angle-resolved $I_{\text{SB}}(\theta, \tau)$ XUV-IR ionization of the outer p subshell of Ar($3p^6$) and Ne($2p^6$). The experiment combines the RABBITT scheme implemented at the 10 kHz beamline of the new Attolab facility and electron-ion coincidence 3D momentum spectroscopy based on a Cold Target Recoil Ion Momentum Spectrometer (COLTRIMS) type set-up [50]. Using 25 fs IR pulses at the fundamental wavelength of 800 nm to generate the XUV APTs, the SBs and HHs, producing photoelectrons in the 0-20 eV energy range of interest for this study, do not involve resonant excitation of autoionizing states of Ar [51] or Ne in the continuum and they lie at energies lower than the Ar($3p$) Cooper minimum [52,53]. Therefore, the reported results constitute a probe of the electron dynamics in the continuum populated through direct photoionization of the valence p orbitals in Ar and Ne, where the spin-orbit effects can be neglected [52,53]. However, it was first evidenced in XUV synchrotron radiation studies that, despite their similar character, ionization of np outer-shells of Ne and Ar, governed by the interference of εs and εd angular momentum channels in the continuum [52–55], differ by the role of electronic correlation in the ground state and in the continuum, more prominent for Ar than for Ne. The development of experiments giving access to the temporal dynamics of PI at the attosecond time scale has revived interest for such comparative studies, with the aim to achieve a deeper understanding into the role of electronic correlation and many particle effects in PI [19]. The reported angle-resolved RABBITT experiments provide new information on the complex transition amplitudes associated with the quantum paths defined by a given intermediate and final state in XUV-IR ionization of the outer p subshell of Ar($3p^6$) and Ne($2p^6$). Beyond the $I_{\text{SB}}(\theta, \tau)$ PADs, the angular analysis of the dressed harmonic peaks, HH^{IR} in the presence of the IR field, is also considered.

Complementary to the XUV-IR time resolved studies at the Attolab beamline, we report spectrally resolved PADs for one-photon PI of Ar and Ne in the same energy range, taking advantage of the high-resolution synchrotron SOLEIL facility, obtained with the same end station set up.

The organization of the paper is as follows. In section 2 we present the general form of the $I_{\text{SB}}(\theta, \tau)$ PAD used throughout this work, while the experimental method is described in section 3. Section 4 focuses on the results obtained on valence ionization of Ar and Ne, where we first report a complete set of observables for a pair of SBs corresponding to similar electron energies, and then discuss their energy dependence. Section 5 briefly introduces the theoretical formulation of $I_{\text{SB}}(\theta, \tau)$ in terms of the transition matrix elements, further developed in sections V-VI-Supplementary material (SM), and subsequent properties of the PAD observables. A detailed comparison of the present results with previous measurements

and theoretical calculations is discussed in section 6, prior to the summary and conclusion given in section 7.

2. General form of the $I_{\text{SB}}(\theta, \tau)$ PAD

2.1 $I_{\text{SB}}(\theta, \tau)$: a reduced set of (a_i, b_i, ϕ_i) parameters

The most general expansion of a PAD for a multiphoton process can be written as [56,57]:

$$I(\theta, \phi, \tau) \propto \sum_{L=0}^{L_{\text{max}}} \sum_{M=-L}^L B_{LM}(\tau) Y_{LM}(\theta, \phi), \quad (3)$$

where $Y_{LM}(\theta, \phi)$ denotes the spherical harmonics. The B_{LM} coefficients characterize the photoionization dynamics and, in the present case, they carry the dependence in delay τ . This expression results from the interference of pairs of photoelectron partial waves, characterized by orbital angular momenta l and l' , with $L=l+l'$ and M varying from $-L$ to L . In laboratory frame studies, with randomly oriented gas targets, L_{max} is related to the number of photons involved in the ionization process. For XUV-IR two-photon ionization of unaligned atoms induced by linearly polarized XUV and IR fields parallel to each other, $L_{\text{max}} = 4$ and the PAD is independent on the azimuthal angle ϕ . Thus the $I_{\text{SB}}(\theta, \tau)$ PAD for each sideband (equation (2)) can be written as a Legendre polynomial expansion in θ up to the fourth order in the general form:

$$I_{\text{SB}}(\theta, \tau) = h_0(\tau) + h_2(\tau)P_2(\cos\theta) + h_4(\tau)P_4(\cos\theta). \quad (4)$$

The $h_0(\tau)$, $h_2(\tau)$, $h_4(\tau)$ functions of the delay τ are the projections of the $I_{\text{SB}}(\theta, \tau)$ PAD onto the $P_0(\cos\theta)$, $P_2(\cos\theta)$ and $P_4(\cos\theta)$ Legendre polynomials and are expanded in terms of trigonometric basis sets as:

$$\begin{aligned} h_0(\tau) &= a_0 + b_0 \cos(2\omega\tau + \phi_0) \\ h_2(\tau) &= a_2 + b_2 \cos(2\omega\tau + \phi_2) . \\ h_4(\tau) &= a_4 + b_4 \cos(2\omega\tau + \phi_4) \end{aligned} \quad (5)$$

The (a_i, b_i, ϕ_i) parameters (for $i = 0, 2, 4$) are determined by applying a Fourier transform of the $h_i(\tau)$ functions. $h_0(\tau)$ represents the $I_{\text{SB}}(\tau)$ angle-integrated SB intensity, a_0 its mean value, b_0 the amplitude of the oscillatory term and ϕ_0 a phase origin, specific to each SB, which corresponds to the $\Delta\phi$ phase shift in equation (1). $h_2(\tau)$ and $h_4(\tau)$ feature the terms weighting the angular components of $I_{\text{SB}}(\theta, \tau)$ of second and fourth Legendre polynomial orders, characterized by their mean values a_2, a_4 , their magnitudes b_2, b_4 ($b_i \geq 0$) and phases ϕ_2 and ϕ_4 of the $2\omega\tau$ oscillatory terms.

The sets of nine (a_i, b_i, ϕ_i) parameters provide the most complete description of the $I_{\text{SB}}(\theta, \tau)$ PAD for a series of SBs. For a given SB, different measured or computed PADs can be compared by normalizing on the mean value a_0 ($a_0 = 1$) and

choosing a fixed phase origin (ϕ_0), further reducing to seven significant ($a_2, a_4, b_0, b_2, b_4, \phi_{20}$ and ϕ_{40}) parameters. In the ϕ_{20}, ϕ_{40} phase shifts of $h_2(\tau)$ and $h_4(\tau)$ relative to the isotropic signal $h_0(\tau)$, $\phi_{20} = \phi_2 - \phi_0$, $\phi_{40} = \phi_4 - \phi_0$, the contribution of the attochirp ($\Delta\phi_{XUV}$) is obviously cancelled.

2.2 Undulation rate and anisotropy parameters

For each SB referenced to a_0 and ϕ_0 , the $I_{SB}(\theta, \tau)$ PAD combining equations (4) and (5) can equivalently be described introducing the undulation rate $R (= b_0/a_0)$ of $h_0(\tau)$, the usual asymmetry parameters β_2, β_4 characterizing its static component (or delay-integrated angular distribution):

$$\beta_2 = \frac{a_2}{a_0}, \quad \beta_4 = \frac{a_4}{a_0} \quad (6)$$

and the anisotropy parameters γ_2, γ_4 , characterizing its delay-dependent component:

$$\gamma_2 = \frac{b_2}{b_0}, \quad \gamma_4 = \frac{b_4}{b_0}. \quad (7)$$

Therefore, the $I_{SB}(\theta, \tau)$ PAD is as well characterized by the seven parameters ($R, \beta_2, \beta_4, \gamma_2, \gamma_4, \phi_{20}, \phi_{40}$).

A similar formal description in terms of (a_i, b_i, ϕ_i) parameters or ($R, \beta_2, \beta_4, \gamma_2, \gamma_4, \phi_{20}, \phi_{40}$) can be applied to the analysis of the HH^{IR} processes in the presence of the dressing IR laser.

Finally, delay-dependent asymmetry parameters $\tilde{\beta}_2(\tau)$ and $\tilde{\beta}_4(\tau)$ are introduced according to equation (4) and written as:

$$\tilde{\beta}_2(\tau) = \frac{h_2(\tau)}{h_0(\tau)} = \frac{\beta_2 + R \gamma_2 \cos(2\omega\tau + \phi_2)}{1 + R \cos(2\omega\tau + \phi_0)}$$

and

$$\tilde{\beta}_4(\tau) = \frac{h_4(\tau)}{h_0(\tau)} = \frac{\beta_4 + R \gamma_4 \cos(2\omega\tau + \phi_4)}{1 + R \cos(2\omega\tau + \phi_0)} \quad (8)$$

2.3 Extraction of dipole matrix elements

We emphasize that the (a_i, b_i, ϕ_i) parameters are expressed in terms of the complex dipole matrix elements for the two-photon transitions from the initial bound state l' to the final continuum state of angular momentum l , noted as $(M_{l'\lambda l}^m)_{2q\mp 1}^\pm$ at the relevant photon energies, where λ features the angular momentum of the intermediate state, m is the magnetic quantum number of the final state and the \pm symbol refers to the IR absorption or emission pathways for each sideband, involving (HH_{2q-1}) or (HH_{2q+1}) harmonics, respectively.

In this study of two-photon ionization of Ar($3p^6$) and Ne($2p^6$), induced by parallel linearly polarized light, the

transitions involve the initial state ($l' = 1; m' = 0, \pm 1$), the continuum intermediate state ($\lambda = 0 \mu = 0; \lambda = 2 \mu = 0, \pm 1$) and the continuum final state ($l = 1, 3; m = 0, \pm 1$) (figure 1), according to the effective selection rules $\Delta l = \pm 1$ and $\Delta m = 0$. The relevant paths for the considered RABBITT scheme are featured in figure 1, and write as (psp) $^\pm$, (pdp) $^\pm$ and (pdf) $^\pm$. Each of these ionization channels ($l'\lambda l$) $^\pm$ is characterized by a transition matrix element $(M_{l'\lambda l}^m)_{2q\mp 1}^\pm$ with a magnitude $\sigma_{l'\lambda l}^\pm$ and a total phase after the two-photon ionization $\delta_{l'\lambda l}^\pm$. The procedure leading to the expression of the $h_i(\tau)$ functions in terms of these parameters is described in section V-SM and VI-SM and some subsequent properties of the $h_i(\tau)$ functions are discussed in section 5.

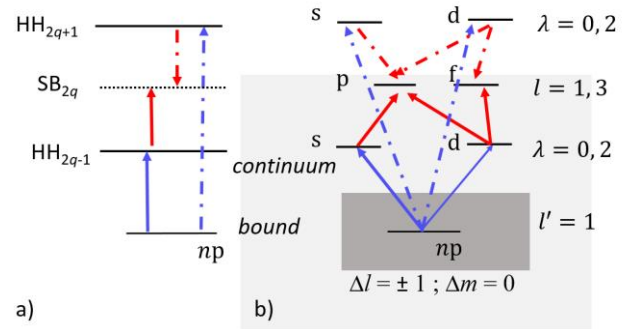


Figure 1 Schematic representation of the interferometric RABBITT scheme for ionization of the valence np subshell of Ar or Ne. Blue arrows represent the XUV photon ionization step and red arrows represent the continuum-continuum transitions induced by an IR photon. Solid lines feature the absorption pathway ($HH_{2q-1}+IR$) and dotted-dashed lines denote the emission pathway ($HH_{2q+1}-IR$) leading to the same final state denoted by SB_{2q} .

3. Experimental method

The experiments were performed at the FemtoAttoBeamline (FAB10) of the new Attolab facility, using the very broad band (VBB) branch, as schematized in figure 2. On FAB10, the amplified Titanium Sapphire IR driving laser (10 kHz, 2 mJ, 25 fs, 800 nm) focused onto an Ar target generates an XUV attosecond pulse train (APT) corresponding to a frequency comb of odd high-order harmonics of the fundamental laser of angular frequency ω . The APT transmitted through an aluminium filter (LUXEL R/N 35220 213.5nm Meshless/Al frame) ($HH_{11}-HH_{25}$) is first focused at the interaction region of a magnetic bottle TOF spectrometer, using a set of two gold coated plane and toroidal mirrors at grazing incidence. There it is superimposed with a phase-locked IR dressing field, of weak intensity (\approx few 10^{11} W/cm 2), whose delay τ relative to the driving laser field can be controlled at the attosecond time scale using a stick-and-slip delay line (SmarAct SLC 2430S s). This sets the conditions for applying the standard RABBITT interferometric technique to two-photon photoionization of a chosen gas target. Using a second toroidal mirror at grazing incidence, the synchronized superposition of the APT and IR

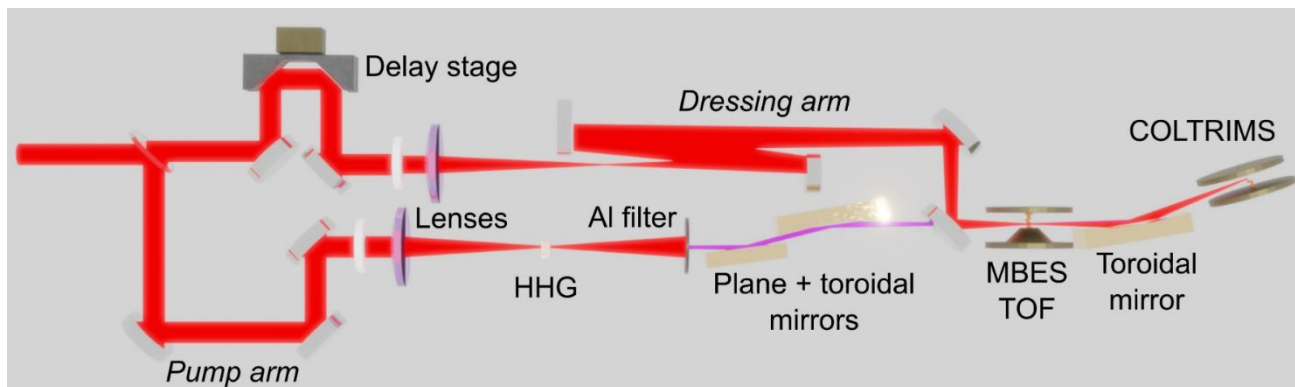


Figure 2 Experimental set-up: A 10 kHz, 2 mJ, 25 fs, 800 nm IR laser is split into pump and dressing arms. The driving IR laser is focused onto the Ar gas target, generating harmonics, which are spectrally filtered and later recombined with the less intense, coherent, dressing IR beam, using a drilled mirror. The two-photon RABBITT scheme is realized after focussing the XUV and IR beams, with a controlled delay between the two fields in the subfemtosecond time scale, into the magnetic bottle electron spectrometer and subsequently into the COLTRIMS spectrometer.

dressing laser is then replicated at the center of a 3D electron-ion coincidence momentum spectrometer allowing for angularly resolved two-photon ionization in the RABBITT scheme. During this commissioning stage of FAB10, the delay τ was not actively stabilized.

The CIEL COLTRIMS-type set-up, derived from previous versions [58,59], combines a two-skimmer supersonic expansion with a coincidence electron-ion momentum spectrometer. A set of electrostatic and magnetic fields is used to guide electrons and ions towards their respective time and position sensitive delay line detectors (DLD-80 PSDs RoentDek), together with an electrostatic lens for focusing energetic ion trajectories when dissociative ionization of molecules is studied [28,60,61]. A multichannel time to digital converter that encodes the DLD time signals, providing the position for each particle of the (A^+, e^-) coincident events as well as the ion time of flight (TOF), while the electron TOF is measured using a synchronized time to amplitude converter (TAC) [60]. Knowing the (v_x, v_y, v_z) components of the emission velocity vector, one gets access to the kinetic energy as well as to the relevant emission polar and azimuthal angles for each particle. Coincidence detection of photoelectrons and ions was used here to obtain a clean electron signal and discriminate against the contribution of residual gas in the interaction region. It also allows for a correction of the velocity vectors based on momentum conservation.

For photoionization of atomic gases, the experiment gives access to the PAD $I(\theta, \tau)$ for each SB or HH peak selected in the photoelectron spectra, where θ is the emission polar angle relative to the light polarization axis \mathbf{P} . At the 10 kHz repetition rate of the driving IR laser available on FAB10, the overall coincidence count rate was restricted to about 500 c/s (0.05 events per pulse) in order to ensure valid coincidences. The subsequent statistics for the measurements presented for photoionization of Ar and Ne rare gases is discussed in the next sections. Typically, an extraction field of 8 V/cm and a magnetic field of 7.52 G, ensuring a 4π collection of electrons up to an energy of 15 eV, were used.

The polarimetry analysis of the XUV-only HH peaks in the PES, based on PADs analyzed in the laboratory frame, or in the molecular frame (MFPADs) [61,62], revealed a polarization state described in terms of the Stokes parameters [63] by a degree of linear polarization of the order of $s_1 \approx 0.92$, a weak contribution of elliptically polarized light ($s_3 \approx 0.15$) and unpolarized light ($s_4 \approx 0.07$). The static asymmetry parameters reported in the next sections are corrected from this polarization defect when specified. The influence on the delay-dependent observables would require further studies.

Typical PESs measured in CIEL for the studied two-photon ionization of the ground state of Argon (IP = 15.76 eV) and Neon (IP = 21.56 eV) atoms as displayed in figure 1-SM, show contributions from HHs and SBs for electrons up to a kinetic energy of about 20 eV. For the reported data, a 4π angular collection of photoelectrons was ensured up to $E_e = 15$ eV. In this energy range, the relative intensity of the HH peaks resolved in the PESs for XUV-only PI (in the absence of dressing IR laser) (figure 1-SM(a) for Ar and figure 1-SM(b) for Ne) is governed by the convolution of the transmitted HHG spectra and the cross sections for ionization of the 3p and 2p valence orbitals of Ar and Ne, respectively. A small contribution arising from 3s ionization of Ar (IP = 29.24 eV) induced by higher HHs was identified at the lowest photoelectron energies and their contribution to the studied SBs can be evaluated, consistent with the $Ar(3s^{-1})$ and $Ar(3p^{-1})$ cross sections. In figure 1-SM(c) and (d), the PESs displaying SBs and HH^{IR} s for Ar and Ne in the presence of the dressing IR laser are averaged over the delay τ .

The data analysis procedure to obtain the $I_{SB}(\theta, \tau)$ PADs is described in the section II-SM. The angle-resolved RABBITT results presented in section 4 correspond to SB_{14} - SB_{20} for Ar and SB_{16} - SB_{22} for Ne. The contribution of each selected SB or HH is obtained by integrating the number of counts within a narrow energy window (± 0.6 eV), in order to limit the effects of the partial overlap between neighbour peaks in the PES. The intensity of the SBs and the HH^{IR} peaks as a function of

the delay are analyzed as $h_0(\tau)$: they display similar oscillations but opposite phases, the integral ionization yield of the PES (sum of SBs and HH^{IR}s) being independent on τ .

4. Results

4.1 Complete description of the $I_{SB}(\theta, \tau)$ PADs for SB_{16}^{Ar} and SB_{20}^{Ne}

In this section we report the complete set of observables describing the PADs for SB_{16} in Ar (SB_{16}^{Ar}) and SB_{20} in Ne (SB_{20}^{Ne}), which correspond to a comparable photoelectron energy of $E_e=9.04\text{eV}$ (SB_{16}^{Ar}) and $E_e=9.44\text{eV}$ (SB_{20}^{Ne}). The full description of the SB signal is given in terms of the three $h_i(\tau)$ functions (for $i = 0, 2, 4$) (equations (4-5)). They are presented for SB_{16}^{Ar} and SB_{20}^{Ne} in figure 3 for a single period of the SB oscillation, choosing a normalization $a_0 = 1$ and a common phase origin ϕ_0 for Ar and Ne to facilitate the comparison. The corresponding sets of extracted (a_i, b_i, ϕ_i) parameters are reported in Table 1 with related statistical uncertainties.

The angle-integrated signal $h_0(\tau)$ is found to be comparable for both Ar and Ne, with a similar magnitude of the oscillatory term $b_0^{Ar/Ne}$ or undulation rate R . These values, comparable to that measured for Ar in the magnetic bottle spectrometer during the experiments, are in the range of previously reported results (e.g. $R \approx 0.3$ extracted from ref. [2] for SB_{16}^{Ar}). The $h_2(\tau)$ functions oscillate with a similar magnitude $b_2^{Ar/Ne}$ around a mean value $a_2^{Ar/Ne}$ which differs for Ar and Ne due to different static asymmetry parameters (see section 4.2). We observe that the phase shifts $\phi_{20}^{Ar/Ne}$ are relatively small in both cases. The $h_4(\tau)$ oscillatory functions provide similar parameters for the fourth order Legendre polynomial components. a_4^{Ar} and a_4^{Ne} are rather weak and display opposite signs, negative for the Ne case. The $\phi_{40}^{Ar/Ne}$ phases display a remarkable difference since for ionization of Ne, $h_4(\tau)$ oscillates with a phase shift of π relative to $h_0(\tau)$.

Accordingly, the undulation rate, asymmetry parameters and phase shifts ($R, \beta_2, \beta_4, \gamma_2, \gamma_4, \phi_{20}, \phi_{40}$), retrieved from the (a_i, b_i, ϕ_i) parameters as defined in section 2.2, are summarized in table 1-SM. They are included and discussed in detail in section 4.2 and section III-SM illustrating the energy dependence of the $I_{SB}(\theta, \tau)$ PADs.

The consistent set of $A(\theta), B(\theta), C(\theta)$ functions describing the $I_{SB}(\theta, \tau)$ PAD for SB_{16}^{Ar} and SB_{20}^{Ne} in equation (2), derived from the set of (a_i, b_i, ϕ_i) as given in section I-SM, are reported and discussed in figure 2-SM.

As a summary of the delay and angular dependence of the SB signal, illustrated for SB_{16}^{Ar} , the bidimensional colour plot of the $I_{SB}(\theta, \tau)$ PAD built up from the (a_i, b_i, ϕ_i) parameters is displayed in figure 4 for a single period of the SB oscillation. The projections of the 2D $I_{SB}(\theta, \tau)$ PAD onto the x and y axes correspond to the angle-integrated $I_{SB}(\tau) = h_0(\tau)$ intensity

(figure 3(a)) and to the delay-integrated $I_{SB}(\theta) = A(\theta)$ PAD (see figure 2(a)-SM), respectively. The white dashed line locating

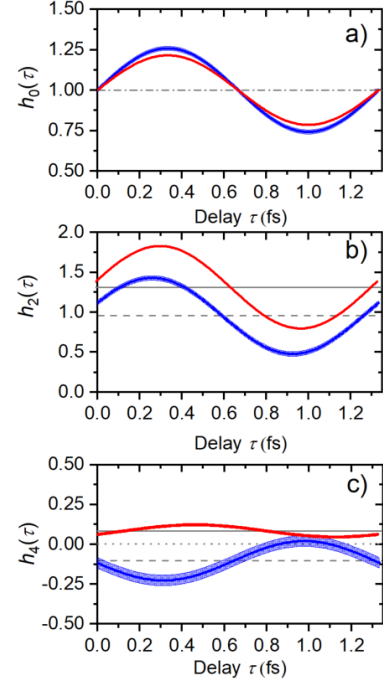


Figure 3 $h_0(\tau), h_2(\tau), h_4(\tau)$ functions for SB_{16}^{Ar} (red) and SB_{20}^{Ne} (blue), normalized with $a_0 = 1$ and a common phase origin ϕ_0 . The band thickness features the statistical uncertainty (\pm one standard deviation) deduced from the chi-square of the fit. The solid (dashed) horizontal lines indicate the mean value of each $h_i(\tau)$ for Ar (Ne).

(a)	a_i	b_i	ϕ_{i0}
h_0	1	0.210[0.002]	0
h_2	1.31[0.01]	0.52[0.01]	0.13[0.01]
h_4	0.08[0.01]	0.04[0.01]	-0.63[0.15]

(b)	a_i	b_i	ϕ_{i0}
h_0	1	0.26[0.02]	0
h_2	0.950[0.025]	0.48[0.06]	0.35[0.04]
h_4	-0.10[0.045]	0.12[0.03]	3.24[0.36]

Table 1. The (a_i, b_i, ϕ_i) parameters (for $i = 0, 2, 4$) for SB_{16}^{Ar} (a) and SB_{20}^{Ne} (b). Error bars represent \pm one standard deviation as obtained by analyzing the series of individual measurements.

the maximum of the SB signal for each angle θ features the variation of the atomic time delay $\tau_A(\theta) = C(\theta)/2\omega$ in the range $0-180^\circ$ relative to $\tau_A(0^\circ)$. $\tau_A(\theta)$ remains about zero up to about 60° and encounters a steep drop for larger angles reaching here a delay of the order of -500 as at 90° , with a symmetric variation between 90° and 180° . We refer to figure 2-SM(c) for a detailed comparison of SB_{16}^{Ar} and SB_{20}^{Ne} .

The delay-dependent asymmetry parameters $\tilde{\beta}_2(\tau)$ and $\tilde{\beta}_4(\tau)$ which quantify the θ dependence for each delay τ , obtained from equation (8), are displayed in figure 5 for SB_{16}^{Ar} . They oscillate with a frequency of 2ω and an amplitude of

$\beta_{2/4\text{amp}}$ ($\beta_{2\text{amp}}^{\text{Ar}}=0.25$, $\beta_{2\text{amp}}^{\text{Ne}}=0.27$). The comparison of these parameters for $\text{SB}_{16}^{\text{Ar}}$ and $\text{SB}_{20}^{\text{Ne}}$ is presented in figure 3-SM.

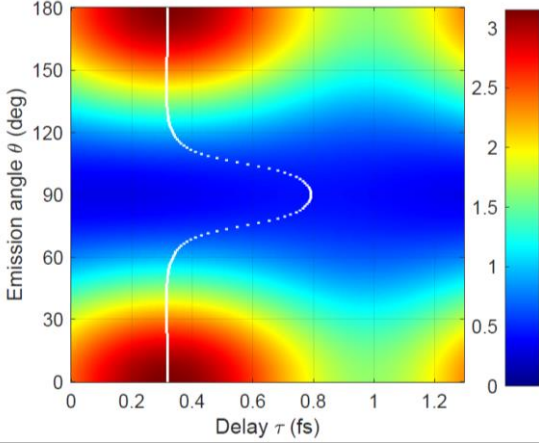


Figure 4 $I_{\text{SB}}(\theta, \tau)$ PAD bidimensional histogram for a single period of $\text{SB}_{16}^{\text{Ar}}$ oscillation as a function of the XUV-IR delay τ and the polar emission angle θ . The white dashed line, for each θ , is the location of the maxima of $I_{\text{SB}}(\theta, \tau)$ featuring the $C(\theta)$ phase.

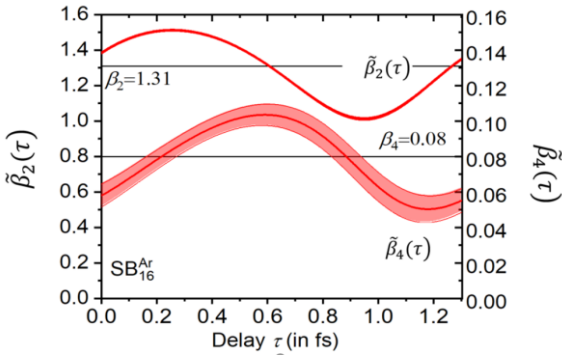


Figure 5 Evolution of $\tilde{\beta}_2(\tau)$ and $\tilde{\beta}_4(\tau)$ for $\text{SB}_{16}^{\text{Ar}}$. Their mean value differs slightly from the delay-independent (static) asymmetry parameters β_2 and β_4 whose values are indicated as solid horizontal lines.

4.2 Electron energy dependence of the observables

In order to characterize the evolution of the $I_{\text{SB}}(\theta, \tau)$ PAD with the photon or photoelectron energy for $\text{SB}_{14}\text{-SB}_{20}$ for Ar and $\text{SB}_{16}\text{-SB}_{22}$ for Ne, we present in this section the $\beta_{2/4}$ asymmetry parameters and the $\gamma_{2/4}$ anisotropy parameters as defined in section 2.2, as well as the phase shifts ϕ_{20} and ϕ_{40} . For completeness, we also report similar parameters extracted from the analysis of the $I_{\text{HH}}(\theta, \tau)$ PADs for the dressed HH^{IR} peaks, subsequent to the depletion of the XUV-only HH peaks. The energy dependence of the R undulation rate and that of the ϕ_0 phase, which partially characterize the experimental conditions of the measurements including the group delay of the XUV-APT, are reported in section III(b)-SM, as well as other derived observables such as the atomic time delays $\tau_{\text{A}}(\theta)$.

Figure 6 displays the evolution of the $\beta_{2/4}$ asymmetry parameters describing the delay-independent component of

the $I(\theta, \tau)$ PADs for the respective SBs and HH^{IR} s for two-photon ionization of Ar and Ne, as a function of photoelectron energy. It also includes the β_2^{SR} asymmetry parameters measured for one-photon ionization at Synchrotron SOLEIL, in very good agreement with previous measurements [54,55,64]. We note that this statement applies as well to the detailed region of the $3s^23p^6 \rightarrow 3s3p^6np$ ($n=4$) autoionizing resonance (section IV-SM). The β_2^{XUV} parameters measured at Attolab for XUV-only PI of Ar and Ne in parallel experiments (not shown) were found lower by about 6%, which is consistent with the partial depolarization of the XUV light beam evaluated by the polarimetry analysis. The values reported in figure 6 are corrected accordingly (see section 3).

As a general trend, β_2^{SB} increases with the photoelectron energy with a slope comparable to that observed for β_2^{SR} (or β_2^{HH}). For both targets, the measured β_2^{SB} values are significantly larger than those of $\beta_2^{\text{HH-IR}}$ and β_2^{HH} for the neighboring harmonics, whatever the positive or negative sign of the β_2^{HH} asymmetry parameter characterizing the XUV-only PAD at the corresponding photon energy. This enhancement, remarkably stronger for Ne than for Ar, describes the significant alignment of the SB PADs favoring electron emission in the direction of the polarization axis. The values found for $\beta_2^{\text{HH-IR}}$, lower than β_2^{HH} indicate that depletion of the HH peaks results in a modified PAD, which then a priori, also implies the contribution of a fourth order Legendre polynomial. β_4^{SB} and $\beta_4^{\text{HH-IR}}$ take rather weak values at the explored energies. Within uncertainties, they show a weak variation when turning from SBs to HH^{IR} s, featuring a small decrease or increase in the range -0.2 to 0.2 for Ar and Ne, respectively, within a rather flat energy dependence. These characteristics are further discussed in section 6.

The evolution of the anisotropy parameters γ_2 and γ_4 and relative phases ϕ_{20} and ϕ_{40} characterizing the delay-dependent component of the SB and HH^{IR} PADs as a function of the photoelectron energy is shown in figure 7 for Ar and Ne. The rather large and comparable values of γ_2 , in the range of 2.5 for Ar and 2 for Ne, correspond to a significant angular anisotropy, weakly dependent on the photoelectron energy. Here again the anisotropy is lower for the fourth order Legendre polynomial term, with γ_4 ranging around 0.2 for Ar, and 0.5 for Ne with an increase found at the smaller energies. The $\phi_{20}^{\text{Ar/Ne}}$ and $\phi_{40}^{\text{Ar/Ne}}$ phase shifts referenced to the angle-integrated signal remain relatively small in the explored energy range, with the exception of ϕ_{20}^{Ne} at low energy and that of ϕ_{40}^{Ne} which remains rather stable around the value of π . With a larger γ_2 parameter, even small changes in $\phi_{20}^{\text{Ar/Ne}}$ between 0 to 0.3 rad, are reflected in the anisotropies seen in the delay-dependent component of the SB signal.

The corresponding characteristics of the $\tilde{\beta}_2(\tau)$ and $\tilde{\beta}_4(\tau)$ delay-dependent asymmetry parameters of the SB signal are given in figure 6-SM. Finally, the angular dependence of the atomic delays relative to $\theta = 0^\circ$ for the studied SBs is reported

in figure 5-SM for three series of SBs corresponding to similar photoelectron energies, namely (a) SB_{14}^{Ar} and SB_{18}^{Ne} (b) SB_{16}^{Ar} and SB_{20}^{Ne} (c) SB_{18}^{Ar} and SB_{22}^{Ne} . As a general trend, we observe

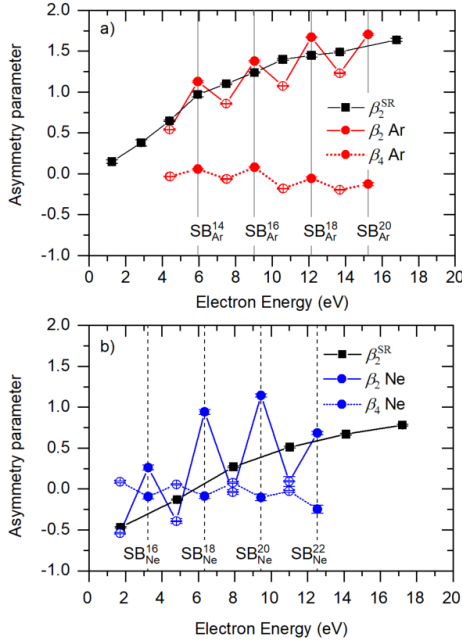


Figure 6 Evolution of β_2^{SB} , β_4^{SB} (solid circle) and β_2^{HH-IR} , β_4^{HH-IR} (open circle) for two-photon ionization of Ar (a) and Ne (b), as a function of the electron energy. β_2^{SR} (black squares): asymmetry parameters measured at Synchrotron SOLEIL for one-photon ionization of Ar and Ne, comparable to the β_2^{HH} values for XUV-only ionization induced by the APT (not shown). Error bars represent \pm one standard deviation as obtained by analyzing the series of individual measurements.

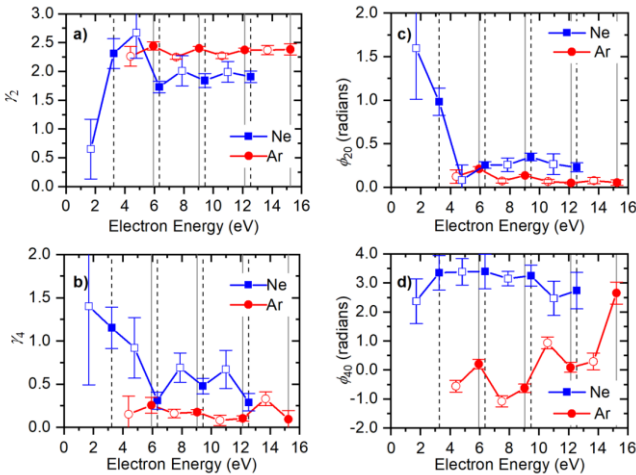


Figure 7 Variation of the anisotropy parameters γ_2 (a), γ_4 (b) and phase shifts ϕ_{20} (c), ϕ_{40} (d) characterizing the delay-dependent component of the SBs (full symbols) and HH_{IRS} (open symbols) as a function of the electron energy for Ne (blue square) and Ar (red circle). Vertical lines (dashed: SB_{Ne} ; solid: SB_{Ar}) feature the position of the SB Electron energies. Error bars represent \pm one standard deviation as obtained by analyzing the series of individual measurements.

that the magnitude of the atomic delays at small ejection angles is larger for Ne than for Ar, while it reaches larger values for Ar at angles greater than $\theta = 70^\circ$. We also observe that the lowest SBs (SB_{14}^{Ar} and SB_{16}^{Ne}) show a larger emission anisotropy for smaller emission angles in both cases.

5. Development of the $h_i(\tau)$ functions and related properties of the parametrized $I_{SB}(\theta, \tau)$ PADs

The $h_i(\tau)$ functions characterizing the $I_{SB}(\theta, \tau)$ PAD are expressed in terms of the complex dipole matrix elements for each ionization channel, as reported in section VI-SM. The latter consist of the magnitude $\sigma_{l'\lambda l}^\pm$ of the radial part of the matrix elements and the phase term $\delta_{l'\lambda l}^\pm$, ($=\Phi_{l'\lambda l}^\pm + \eta_l + \phi_{2q\mp 1}$), including the phase of the radial part of the matrix element ($\Phi_{l'\lambda l}^\pm$), the l dependent radial phase shift η_l and the harmonic phases $\phi_{2q\mp 1}$, i.e. six amplitudes and six phases for the studied XUV-IR PI reactions (section 2.3). The theoretical description is based on second-order perturbation theory [35], summing coherently the transition amplitudes corresponding to the (\pm) pathways for each intermediate state λ , for all degenerate states (m'). Here, we show that the development of the $h_i(\tau)$ functions in equations (14-SM to 16-SM) (i) leads to some basic properties of the $I_{SB}(\theta, \tau)$ PAD parametrized by the (a_i, b_i, ϕ_i) or ($R, \beta_2, \beta_4, \gamma_2, \gamma_4, \phi_{20}, \phi_{40}$) observables, and (ii) enables us to discuss to which extent the outcome of angle-resolved RABBITT two-photon photoionization constitutes a complete experiment, i.e., is likely to provide all the dynamical parameters [56,57,65]. Both statements support the subsequent discussion in section 6.

5.1 Properties derived from the development of the $h_i(\tau)$ functions

The first outcome of the development of the $h_i(\tau)$ functions in equations (14-SM to 16-SM) is to provide a detailed comparison of the measured (a_i, b_i, ϕ_i) parameters and, building on these, of any observable characterizing the PAD, with theoretical calculations providing the complex two-photon transition matrix elements for the $(l'\lambda l)^\pm$ channels. As for the comparison between different experimental results, it enables us to emphasize the dependence of PAD observables onto specific conditions characterizing the instrumental context. This arises, e.g., if the intensities of the successive harmonics involved in the RABBITT oscillation scaled by $|E_{2q-1}|$ and $|E_{2q+1}|$ differ as shown in section VI-SM. As a consequence, the undulation factor R , the static β_2, β_4 as well as the delay-dependent $\tilde{\beta}_2(\tau), \tilde{\beta}_4(\tau)$ asymmetry parameters, are dependent on the relative intensities of the HHs, while the γ_2, γ_4 parameters and the ϕ_{20} and ϕ_{40} phases depend only on the atomic matrix elements.

The expressions of h_0, h_2 and h_4 illustrate two additional properties. Firstly, the τ integrated $I_{SB}(\theta)$ PAD (characterized

by the a_0, a_2, a_4 terms) shows explicitly the correspondence between the RABBITT scheme and XUV-IR two-color two-photon “*interference-free*” ATI, as studied in earlier PAD experiments and calculations for ATI sidebands of Ar($3p^6$) [27,47] or Ne($2p^6$) [66], where the primary ionization was induced by a filtered harmonic [27] or by FEL radiation [66]. In the RABBITT scheme, $I_{\text{SB}}(\theta)$ corresponds to the incoherent sum of the PADs associated with the positive (IR absorption from HH_{2q-1}) and negative (IR emission from HH_{2q+1}) ATI sidebands [27,47]. The determination of a_0, a_2, a_4 provides three equations involving the dynamical parameters which characterize the $(l'\lambda)^\pm$ two-photon PI channels, at the HH_{2q-1} or the HH_{2q+1} XUV ionization energy. In particular, the phase terms included therein involve absolute phase differences between either bc or cc phases for $(l' \rightarrow \lambda)$ or $(\lambda \rightarrow l')$ transitions at fixed XUV ionization energy, as reported for He in ref. [33]. Secondly, when the absorption and emission pathways for each channel are described by identical complex transition matrix elements $(M_{l'\lambda}^m)_{2q-1}^+ = (M_{l'\lambda}^m)_{2q+1}^-$, (as in the high kinetic energy SPA regime [4]), or when the magnitudes $|(M_{l'\lambda}^m)_{2q-1}^+| = |(M_{l'\lambda}^m)_{2q+1}^-|$ are equal and all phases get independent on the angular momenta (λ, l) [11], the τ dependence of $h_0(\tau), h_2(\tau)$ and $h_4(\tau)$ and therefore that of $I_{\text{SB}}(\theta, \tau)$ factorize in the form of $(1 + \cos(2\omega\tau + \delta))$, so that the PAD writes as:

$$I_{\text{SB}}(\theta, \tau) \propto I_o \left(1 + \beta_2 P_2(\cos\theta) + \beta_4 P_4(\cos\theta) \right) \cdot (9) \\ (1 + \cos(2\omega\tau + \delta))$$

Consistently, in these cases $\tilde{\beta}_2(\tau)$ and $\tilde{\beta}_4(\tau)$ are independent on τ , and $C(\theta)$ and the atomic time delay $\tau_A(\theta)$, become independent on θ .

5.2 Towards a complete RABBITT experiment

The explicit development of the $h_i(\tau)$ functions addresses the ability to extract the moduli and phases of the dipole matrix elements for all relevant ionization channels, relying on an appropriate cosine fit of the experimental data. For the optical scheme considered here, where the XUV and IR fields have parallel linear polarizations, this task is not at reach for two-photon ionization of a p atomic orbital which involves two intermediate states, s and d (figure 1), since nine equations are obtained through the fit compared with the twelve unknown quantities (six magnitudes and six phases). One simplification arises if one considers the d intermediate state as playing a dominant role in the XUV ionization process consistent with the Fano’s propensity rule for photoionization [67]. Such an assumption reduces the number of unknowns to eight in the expression of the $h_i(\tau)$, as given in section VI(b)-SM, similar to the example of XUV-IR ionization of He discussed recently [33], and could provide matrix elements for

the considered quantum paths. The applicability of these considerations in the present study is discussed in section 6.3.

6. Discussion

Based on the description of $I_{\text{SB}}(\theta, \tau)$ (section 2 and section I-SM) and the properties of the $h_i(\tau)$ functions (section 5 and section VI-SM), we first briefly compare the PADs reported in this work to previous experimental [25,28,31] results available for coherent XUV-IR two-photon ionization of Ar, and to different theoretical calculations involving RABBITT ionization of Ar and Ne [11,34,35,39]. As mentioned earlier, a common normalization of the $I_{\text{SB}}(\theta, \tau)$ PADs is chosen to facilitate such comparisons, setting the mean value of the angle-integrated RABBITT signal $h_0(\tau)$ to $a_0 = 1$. The first relevant parameter to compare different experiments or simulations is the undulation rate R of $h_0(\tau)$. Then, we consider throughout this discussion the PAD observables in terms of the β_2 and β_4 asymmetry parameters characterizing the anisotropy of the τ -integrated differential cross section $A(\theta)$ on the one hand, and in terms of the $\gamma_2, \gamma_4, \phi_{20}$ and ϕ_{40} anisotropy parameters and phase shifts characterizing the oscillatory component of the PAD, on the other hand. The latter parameters provide in particular, the phase $C(\theta)$ i.e. the angular dependence of the atomic time delay $\tau_A(\theta)$. Finally, the $\tilde{\beta}_2(\tau)$ and $\tilde{\beta}_4(\tau)$ functions characterize the parallel τ dependence of the PAD anisotropy.

6.1 Comparison with experimental results

The PADs for XUV-IR ionization of Ar reported in [25] for specific RABBITT-like conditions allow for the most complete comparison with the present results for $\text{SB}_{16}^{\text{Ar}}$, since they are expressed in terms of three functions describing the $I_{\text{SB}}(\theta, \tau)$ expansion in Legendre polynomials, directly comparable with $h_0(\tau), h_2(\tau)$, and $h_4(\tau)$. A cosine fit of these functions of τ according to equation (5) leads to PAD trends, similar to those observed in the present work, although larger anisotropies are obtained in particular for the terms of fourth order β_4 and γ_4 . Table 2 shows the comparison of the parameters of [25] with the present work. The observed deviations also result in a gap between the undulation of $\tilde{\beta}_2(\tau)$ and $\tilde{\beta}_4(\tau)$ characterizing the evolution of the PAD as a function of delay, which amounts to 0.45 (0.13) for $\beta_2(\beta_4)$ [25] compared to 0.25 (0.03) (this work). In order to understand such differences, further investigations need to be pursued ensuring the most precise characterization of the instrumental conditions, e.g., relative intensities of the consecutive harmonics, active stabilization of the XUV-IR delay τ , polarization of XUV/IR.

Although the results reported in [28], using the same COLTRIMS as this experiment, address a higher IR intensity regime (10^{12} W/cm²), the SBs are dominantly associated with absorption of one XUV photon and exchange of a single IR photon and therefore suited for comparison with the present

results. The PADs measured for the two delays τ ensuring maximum (τ_{Max}) or minimum (τ_{min}) intensity of the $\text{SB}_{14}^{\text{Ar}}$ in

	This work	Ref. [25]	Ref.[35]
R	0.21 ± 0.003	0.53 ± 0.03	0.89
β_2	1.37 ± 0.01	1.73 ± 0.05	2.77
β_4	0.08 ± 0.01	0.50 ± 0.02	1.13
γ_2	2.48 ± 0.03	2.30 ± 0.05	2.89
γ_4	0.19 ± 0.03	0.65 ± 0.02	1.11
$\phi_{20}(\text{rad})$	0.13 ± 0.01	0.024 ± 0.07	-0.009
$\phi_{40}(\text{rad})$	-0.63 ± 0.15	0.081 ± 0.08	0.007

Table 2. ($R, \beta_2, \beta_4, \gamma_2, \gamma_4, \phi_{20}, \phi_{40}$) parameters for $\text{SB}_{16}^{\text{Ar}}$ comparing the experimental results of the current work to those (i) extracted from ref. [25]¹ and (ii) based on the theoretical calculations in ref. [35].

XUV-IR ionization of Ar are found to display a very similar shape, consistent with the calculations based on SPA modelling of the experiment. A fit of these PADs [28] returns $\tilde{\beta}_2(\tau_{\text{Max}}) \approx \tilde{\beta}_2(\tau_{\text{min}}) \approx 1.4$, while for $\text{SB}_{14}^{\text{Ar}}$, the present results yield $\tilde{\beta}_2(\tau_{\text{Max}}) \approx 1.29$ and $\tilde{\beta}_2(\tau_{\text{min}}) \approx 0.93$, and an undulation of $\tilde{\beta}_2(\tau)$ of 0.18. The values extracted for β_4 are of the order of 0.1 [28], comparable to the present results.

The RABBITT experiments discussed in [31], focused on the determination of angle-resolved photoionization delays in the presence of resonantly excited Ar^* autoionizing states, using a VMI and a COLTRIMS for selected wavelengths of the driving IR laser around 780 nm. Considering here the SBs, which are not affected by the resonances, i.e., $\text{SB}_{14}^{\text{Ar}}$, $\text{SB}_{20}^{\text{Ar}}$ or $\text{SB}_{22}^{\text{Ar}}$, we first observe that the β_2 and β_4 asymmetry parameters extracted from the delay-integrated PADs in [31] lie in the same range as the present values. On the other hand, while the $\tilde{\beta}_2(\tau)$ undulation in [31] is rather constant for the dressed HH^{IR} s around 0.2-0.3, it takes larger values and displays a significant decrease with the photon energy for the SBs, from 0.7 ($\text{SB}_{14}^{\text{Ar}}$) to 0.1 ($\text{SB}_{22}^{\text{Ar}}$). Such a variation is not found in the results reported herein, where the measured undulation of $\tilde{\beta}_2(\tau)$ lies in the range 0.25-0.15 for the SBs (see figure 6-SM) and 0.1 for the HH^{IR} peaks. We note that a quantitative comparison is not really at hand since the undulation rate R which intervenes in $\tilde{\beta}_2(\tau)$ is not given in [31], and that the observed variation between these overall sets of data could partially be attributed to noted differences in the HHG spectra (see e.g. section VII-SM). As for the $\tau_A(\theta)$ atomic time delays relative to $\tau_A(0^\circ)$, the one measured herein for $\text{SB}_{14}^{\text{Ar}}$ (figure 5-SM(a)) compares quite well with the experimental result in [31]: there the atomic delays $\tau_A(\theta)$ are referenced against the value extracted for a (0° - 30°) sector.

6.2 Comparison with theoretical results

The most complete comparison with theoretical calculations is achieved when the computed complex transition matrix elements between the initial and final states are available for all the $(l'\lambda)^+$ channels. Relying on the general expansion of the $I_{\text{SB}}(\theta, \tau)$ PAD presented in section 5 (and section VI-SM), one can then obtain the computed $h_0(\tau)$, $h_2(\tau)$ and $h_4(\tau)$ functions and associated (a_i, b_i, ϕ_i) parameters. We illustrate such an example in section VII-SM, where the $h_i(\tau)$ functions resulting from the calculation of Toma and Muller [35], based on time-independent second-order perturbation theory and a single active electron potential (SAE), are obtained for XUV-IR PI of the $\text{Ar}(3p)$ subshell. The computed $h_i(\tau)$ selecting $\text{SB}_{16}^{\text{Ar}}$ are reported assuming equal intensities of the consecutive harmonics HH_{15} and HH_{17} (figure 9-SM), as well as the corresponding (a_i, b_i, ϕ_i) parameters, extracted from their cosine fit, normalized with $a_0=1$. These values, given in table 2, reflect significantly higher R undulation rate and anisotropies than found experimentally in this work for both the τ -dependent and τ -independent components of the PAD: most of these deviations cannot be accounted for based on instrumental effects discussed above, including the relative HH_{15} and HH_{17} intensities (e.g., tables 2 and 3-SM). Apart from the instrumental context, other origins may be invoked to interpret such discrepancies, e.g., the limitations inherent to the employed theoretical method which does not include dynamical electronic correlation effects, well identified in PI of atoms such as Ar [43,52]. A similar conclusion was drawn in the study of XUV-IR two-color two-photon ATI of Ar [27,47], where the same calculation [35], successful for the prediction of cross section ratios between positive (IR absorption) and negative (IR emission) ATI sidebands of the HH_{13} and HH_{15} harmonics, showed deviations for the measured PADs. Calculations based on second-order perturbation theory and a SAE potential have also been reported for angle-resolved RABBITT two-photon ionization of $\text{Ne}(2p^6)$ [36] at the low energies explored here, considering the $m=0$ magnetic state.

Subsequent many-body second-order perturbation theory within the frame work of RPAE [43], employed in ref. [31,32] for computing angle-resolved time delays for non-resonant XUV-IR ionization of Ar, describe well the present measurements of $\tau_A(\theta)$ for the relevant SB_{14-16} and SB_{20} . These calculations also provided the $\tilde{\beta}_2(\tau)$ parameters describing the τ -dependent anisotropy of the $I_{\text{SB}}(\theta, \tau)$ PAD for SB_{14-20} [32]. Their comparison with the reported results shows discrepancies, in terms of shape of the $\tilde{\beta}_2(\tau)$ periodic function and the energy dependence of its oscillation amplitude. This could be attributed to a different R undulation rate of the $h_0(\tau)$ angle-integrated SB signal (equation (8)).

Angle-resolved RABBITT two-photon ionization of $\text{Ne}(2p^6)$ and $\text{Ar}(3p^6)$ has also been studied by solving the

¹ Some of the numbers listed for ref. [25] were provided on the occasion of this paper, complementary to the data in [25].

TDSE [34,39], within the SAE approximation, providing the ionization amplitude $a(\mathbf{k})$ for each polar angle θ relative to the polarization and the photoelectron spectrum $|a(\mathbf{k})|^2$. The fit of the computed $I_{SB}(\tau)$ signal in the emission direction \mathbf{k} along with equation (2) provided the $A(\theta)$, $B(\theta)$ and $C(\theta)$ observables. The angular dependence of $A(\theta)$ and $B(\theta)$ was then identified to the form derived within the SPA: $A(\theta), B(\theta) \propto [1 + \beta_{A,B} P_2(\cos\theta)] \cos^2(\theta)$, which predicts a cancellation of electron emission at $\theta = 90^\circ$. This expansion thereby implies a determined relationship between the second and fourth order asymmetry parameters $\beta_{2A(B)}$ and $\beta_{4A(B)}$ which both express in terms of $\beta_{A(B)}$. Besides, $\beta_{A,B}$ are found to be equal to the asymmetry parameter of the one-photon XUV ionization process at the SB energy, β_{HH} . This contradicts the results of our experiments. Subsequently, the calculations [34,39] which lead to rather constant asymmetry parameters around $\beta_{2A} \approx 2.65$ and $\beta_{4A} \approx 0.65$ for $SB_{14}^{Ar}-SB_{20}^{Ar}$ (figure 9 in [34]), and to β_{2A} and β_{4A} asymmetry parameters varying from 1.6 to 2.4 and from -0.5 to 0.5, respectively, for $SB_{16}^{Ne}-SB_{22}^{Ne}$, deviate from the present experimental findings as reported in section 4. On the other hand, considering the angular dependence of the phase term $C(\theta)$, or the atomic time delay $\tau_A(\theta)$ relative to $\tau_A(0^\circ)$ for two-photon ionization of Ar and Ne, we note a fair agreement between the TDSE predictions and the trends of the present results. The $\tau_A(\theta)$ delays computed for SB_{16}^{Ar} and SB_{20}^{Ne} describe well the present results reported in figure 2-SM(c). For Ne, $\tau_A(\theta)$ progressively deviates from zero above 30° , reaches -50 as for $\theta = 60^\circ$, and then drops to about -200 as for $\theta \approx 80^\circ$, while its evolution is weaker for Ar up to $\theta \approx 60^\circ$, then it encounters a similar drop. The computed angular dependence of the atomic time delay lessens with increasing SB order, consistent with the results discussed in section 4 and section III-SM, in particular for Ar. For SB_{20}^{Ar} the computed time delay for Ar changes sign, unlike the present result.

6.3 Interpretation framework

Low order perturbation theory [4,35] provides a frame for the interpretation of the measured or computed $I_{SB}(\theta, \tau)$ PADs, through their analytical expansion based on the two-photon transition matrix elements for emission and absorption pathways. With the determination of the complex matrix elements for the $(l'\lambda)^\pm$ channels the interest is two-fold, focusing on the interpretation of (i) the τ -dependent component of the $I_{SB}(\theta, \tau)$ PAD accessing the temporally resolved dynamics of the electron through the bc and cc transitions, and (ii) that of the τ integrated $I_{SB}(\theta)$ PAD in terms of XUV-IR two-photon ATI dynamics, at the two HH_{2q-1} and HH_{2q+1} energies. Gathering the analysis of both components included in the $h_0(\tau)$, $h_2(\tau)$ and $h_4(\tau)$ functions provides the most complete information.

(i) The temporally resolved dynamics results in the θ dependence of the atomic time delays $\tau_A(\theta)$, as well as the τ dependence of the SB PAD anisotropy, described by the $\tilde{\beta}_2(\tau)$

and $\tilde{\beta}_4(\tau)$ functions. The interpretation framework of such dependencies is usually simplified considering the asymptotic behavior of the electronic wave functions in the cc transition between the intermediate and final continuum states, and assigning the phase $\eta_\lambda^\pm + \phi_{cc}^\pm - \lambda\pi/2$ to each $(l'\lambda)^\pm$ channel [10,11]. In the asymptotic approximation, valid at higher energies, ϕ_{cc} becomes independent of the orbital angular momentum l of the final state. Several origins may be invoked to interpret such θ or τ dependencies, whether the two-photon ionization transition involves a single or two intermediate states.

A common assumption aiming at a qualitative interpretation of the measured or computed time delay anisotropies in two-photon ionization of $Ar(3p^6)$ or $Ne(2p^6)$ is to consider only a single intermediate state for the transition [10,19,39]. It is rationalized by the dominance of the $p \rightarrow d$ relative to the $p \rightarrow s$ channel based on Fano's propensity rules for bound-free transitions [67], supported by different studies of the one-photon photoionization [53,68]. In the low electron energy range investigated herein, RPAE or MCHF calculations [19] suggest that this assumption is even more justified for Ar ($\sigma_{p \rightarrow d}/\sigma_{p \rightarrow s} \approx 10$ for HH_{15}) than for Ne ($\sigma_{p \rightarrow d}/\sigma_{p \rightarrow s} \approx 3$ for HH_{17}) [19]. If the two-photon transition involves a single intermediate state, the origin of the observed $\tau_A(\theta)$ dependence is necessarily assigned to the cc transition. There, a breakdown of the asymptotic approximation, restoring interference effects between p and f partial waves [29,31,39], or an extension of the Fano's propensity rules to the free-free transition linked to the asymmetry between the magnitudes of the $|(M_{l'\lambda}^m)_{2q-1}^+|$ and $|(M_{l'\lambda}^m)_{2q+1}^-|$ two-photon matrix elements as proposed recently [32] can be considered. Assuming a single d intermediate state in the studied ionization processes the description of the $I_{SB}(\theta, \tau)$ PAD reduces to eight quantities describing the four $(pdp)^\pm$ and $(pfp)^\pm$ complex transition moments. A global fit of the $h_0(\tau)$, $h_2(\tau)$ and $h_4(\tau)$ functions leads to nine equations which can then in principle be numerically resolved, since they involve nine unknowns, including the τ_0 origin. An attempt to solve this set of equations did not lead to a solution using the reported experimental results, within the present statistical quality of the data. This negative result may reflect the fact that the starting hypothesis which consists of neglecting the role of the s intermediate state is not valid. We also note that TDSE calculations [37] predict a sizable SB cross section for the $(l = 1, m = 0)$ final state reached through the interfering s and d ionization paths, which dominates that of the $(l = 1, m = \pm 1)$ and $(l = 3, m = \pm 1)$ states in the 0-20 eV energy region above threshold in XUV-IR ionization of Ar, while for Ne the atomic dipole phase is significantly increased for the $(l = 1, m = 0)$ final state in the same energy region, with the main contribution assigned to the ionization through the s state.

At this step, we therefore keep considering that the two s and d intermediate states play a role in the studied transition.

In that case, as discussed in section 5, the τ dependence of the $I_{SB}(\theta, \tau)$ PAD anisotropy may result from the asymmetry between the absorption or emission pathways [32], or from the dependence of the two-photon phase shifts $\delta_{l\lambda}^{\pm}$ on λ (bc) or l (cc) angular momentum components. The latter condition also implies the θ dependence of $\tau_A(\theta)$, mainly governed by the interference of the s and d partial waves in the ionization continuum ($\tau_w(\theta)$) or that of the p and f partial waves ($\tau_{cc}(\theta)$).

(ii) As for the τ -integrated $I_{SB}(\theta)$ PAD, a coherent picture of the observations can be proposed considering that the absorption probability of the IR photon is favored when photoelectron emission following absorption of the XUV photon occurs at small angles relative to the polarization axis common to the XUV and IR fields. In this perspective, IR absorption is expected to result in a SB PAD which differs more drastically from the XUV-PI-PAD when the initial β_2^{HH} value is negative or around zero ($-0.5 \leq \beta_2^{SR} \leq 0.5$ for Ne), than when the initial PAD is already aligned along the polarization axis with a positive value of β_2^{HH} ($0.5 \leq \beta_2^{SR} \leq 1.7$ for Ar). The relative importance of the primary angular distribution induced by XUV photoionization and its modification by the IR field in the determination of the $I_{SB}(\theta, \tau)$ PAD could be modelled e.g., within the SPA [40], considering higher orders developments than discussed earlier [34].

7. Summary and conclusion

The reported angle-resolved RABBITT study of two-photon direct ionization of the np outer orbitals in Ar and Ne, performed at the Attolab facility using the CIEL COLTRIMS-type set-up, addresses the low energy region, up to 20 eV above the ionization threshold, where the electron dynamics results from both electronic correlation in the ground state or in the continuum, and scattering induced by the XUV and IR fields. A consistent study of the one-photon PI at comparable energies was carried out at the synchrotron radiation facility SOLEIL, with the same experimental setup, for both Ar and Ne.

The data analysis based on a general Legendre polynomial expansion of the measured angular distributions, providing a complete description of the $I_{SB}(\theta, \tau)$ PADs of the SBs in terms of nine parameters (a_i, b_i, ϕ_i) (for $i = 0, 2, 4$), enables us to retrieve any observable characterizing both its τ -integrated and oscillatory components. This method has allowed for a detailed comparison with other experimental results, emphasizing some of the relevant parameters which influence the outcome of RABBITT measurements, as well as with theoretical calculations providing the complex two-photon transition matrix elements. Considering the τ -dependent depletion of the harmonics, a similar approach has been applied to analyze the PADs of the HH^{IR} dressed harmonics.

The comparative investigation of the energy dependence of the $I_{SB/HH}(\theta, \tau)$ PADs recorded for sidebands and dressed harmonics assigned to both Ar and Ne targets, demonstrates

similarities and differences in the two-photon non-resonant photoionization dynamics.

Regarding the $I_{SB}(\theta)$ τ -integrated PADs described by the (β_2, β_4) asymmetry parameters, the general trends of the results reported in section 4 emphasize a net enhancement of the anisotropy of the SB PADs described first by the asymmetry parameter β_2^{SB} , relative to that characterizing the one-photon ionization β_2^{SR} (or β_2^{HH}). This effect is found to be remarkably larger for Ne than for Ar. Within the statistical uncertainties affecting the low values recorded for the β_4^{SB} and β_4^{HH-IR} parameters, a distinct oscillation about zero is visible: for Ar, β_4^{SB} is larger than β_4^{HH-IR} , while for Ne the opposite behavior is observed. These static asymmetry parameters differ from the available theoretical predictions. On the other hand, a decrease of the asymmetry parameter for the HH PADs is found, β_2^{HH-IR} lying below β_2^{HH} .

Describing the oscillatory component of the $I_{SB}(\theta, \tau)$ PAD anisotropy, the (γ_2, γ_4) and (ϕ_{20}, ϕ_{40}) anisotropy parameters and phase shifts, together with the undulation rate R , return rather comparable trends for Ar and Ne, weakly dependent on energy except for the lowest HH^{IR} and SB in Ne. The main differences are found between the fourth order angular components, with a larger γ_4 and a noticeable ϕ_{40} phase shift close to π for Ne. These overall features subsequently account for the anisotropy and energy dependencies of the $\tau_A(\theta)$ atomic time delays, and the SB PAD anisotropies described by $\tilde{\beta}_2(\tau)$ and $\tilde{\beta}_4(\tau)$. As discussed in section 6.2, although a satisfactory theoretical description of the $\tau_A(\theta)$ variation is found, it is not the case for the τ dependence of the SB PAD anisotropy, where the agreement between theory and experiment remains qualitative.

Both static and delay-dependent results will benefit from a comparison with advanced theoretical simulations of the RABBITT two-photon process described by second-order perturbation theory, soft-photon approximation, or solving TDSE, accounting for many-body effects in Ar and Ne. On the other hand, the influence of instrumental parameters such as the accurate control of the IR-XUV delay stabilization, the focusing of the XUV and IR beams in the interaction zone, or defaults in the polarization state of the XUV field, should be further studied. The latter can be conveniently controlled using molecular polarimetry [62].

The optimal comparison between experiment and theory for the studied two-photon ionization of a np atomic orbital, at reach if a complete experiment retrieving all complex transition matrix elements is performed, calls for complementary experimental schemes. One strategy in that direction is to perform similar angle-resolved RABBITT experiments using different polarization states of the XUV and IR fields. These include two linearly polarized fields with a control of their relative orientation, as implemented e.g., in the study of negative and positive ATI sidebands in two-color XUV-IR ionization processes (see, e.g. [69,70] and references therein), as well as the use of elliptically polarized or

polarization-shaped laser pulses [36,71]. Such pump-probe geometries break the axial symmetry of the electron emission pattern, leading to PADs function of two polar and azimuthal angles (θ, φ). 3D momentum spectrometry at play using a COLTRIMS-type spectrometer is well adapted for such investigations.

Relying on a similar methodology as reported here, ongoing work focuses on the study of RABBITT XUV-IR two-photon ionization of small molecules such as NO or O₂, angularly resolved in the molecular frame (MF) [21,72–74]. Aiming at the determination of Wigner time delays as a function of the (θ_e, φ_e) emission direction in the MF, for each orientation χ of the molecular axis relative to the polarization (common to the XUV and IR field), the temporal dynamics of the bc and cc transitions in two-photon photoionization in molecules have to be elucidated. Using electron-ion 3D momentum spectroscopy, the strategy to obtain $I_{SB}(\chi, \theta_e, \varphi_e, \tau)$ molecular frame photoelectron angular distributions (MFPADs) takes advantage of dissociative photoionization subsequent to inner-valence shell ionization and extends the analytical description developed in previous studies [75,76].

Acknowledgements

We dedicate this work to the memory of our colleague and friend Bertrand Carré, coordinator of the Attolab Equipex project.

We gratefully acknowledge the OPT2X consortium (Université Paris-Saclay), in particular F. Polack, D. Dennetière of the Optics group at SOLEIL, J. Lenfant, and the ATTO Physics group (Attolab, LIDYL), for the design and realization of the FAB10 beamline (publication in preparation), as well as I. Vadillo-Torre and M. Billon (LIDYL), M. Sebdaoui (SOLEIL Alignment group) for their support in the construction and commissioning of the beamline. We thank J. Guigand, S. Lupone, N. Tournier, O. Moustier (ISMO) for technical support in maintenance of the CIEL set-up. R.R. Lucchese, M. Vrakking, M. Meyer, M. Gisselbrecht are gratefully acknowledged for fruitful scientific exchanges. We are very grateful to M Lebech for his contribution to the SOLEIL measurements, and to J Bozek, PLEIADES-SOLEIL beamline manager, C Nicolas and A Milosavljevic, beamline scientists, E Robert, beamline engineer assistant on PLEIADES beamline, and L Nahon, DESIRS-SOLEIL beamline manager, G. Garcia, beamline scientist, J F Gil, beamline engineer assistant on DESIRS beamline, for a fruitful collaboration. We thank the SOLEIL general staff for smoothly operating the facility.

This work is supported by “Investissements d’Avenir” LabEx PALM (ANR-10-LABX-0039-PALM) and EquipEx ATTOLAB (ANR-11-EQPX-0005-ATTOLAB), as well as by ASPIRE Marie Skłodowska-Curie ITN (EU-H2020 ID: 674960), Lidex OPT2X-2014 Université Paris-Saclay, EU-

H2020-LASERLAB-EUROPE-654148, and Région Ile de France SESAME2015- Pulse-X.

References

- [1] Yin Y-Y *et al* 1992 *Phys. Rev. Lett.* **69** 2353
- [2] Paul P M *et al* 2001 *Science* **292** 1689
- [3] Prince K C *et al* 2016 *Nature Photonics* **10** 176.
- [4] Véniard V, Taïeb R and Maquet A 1996 *Phys. Rev. A* **54** 721
- [5] Muller H G 2002 *Applied Physics B* **74** S17
- [6] Dahlström J M, L’Huillier A and Maquet A 2012 *J. Phys. B: At., Mol. Opt. Phys.* **45** 183001
- [7] Mairesse Y *et al* 2003 *Science* **302** 1540
- [8] López-Martens R *et al* 2005 *Phys. Rev. Lett.* **94** 033001
- [9] Wigner E P 1955 *Phys. Rev.* **98** 145
- [10] Klünder K *et al* 2011 *Phys. Rev. Lett.* **106** 143002
- [11] Dahlström J M *et al* 2013 *Chem. Phys.* **414** 53
- [12] Maquet A, Caillat J and Taïeb R 2014 *J. Phys. B: At. Mol. Opt. Phys.* **47** 204004
- [13] Pazourek R, Nagele S and Burgdörfer J 2015 *Rev. Mod. Phys.* **87** 765
- [14] Guénot D *et al* 2012 *Phys. Rev. A* **85** 053424
- [15] Isinger M *et al* 2017 *Science* **358** 893–6
- [16] Jordan I *et al* 2017 *Phys. Rev. A* **95** 013404
- [17] Haessler S *et al* 2009 *Phys. Rev. A* **80** 011404
- [18] Huppert M *et al* 2016 *Phys. Rev. Lett.* **117** 093001
- [19] Guénot D *et al* 2014 *J. Phys. B: At. Mol. Opt. Phys.* **47** 245602
- [20] Palatchi C *et al* 2014 *J. Phys. B: At. Mol. Opt. Phys.* **47** 245003
- [21] Vos J *et al* 2018 *Science* **360** 1326
- [22] Kotur M *et al* 2016 *Nat Commun* **7** 10566
- [23] Gruson V *et al* 2016 *Science* **354** 734
- [24] Barreau L *et al* 2019 *Phys. Rev. Lett.* **122** 253203
- [25] Aseyev S A *et al* 2003 *Phys. Rev. Lett.* **91** 223902
- [26] Guyétand O *et al* 2005 *J. Phys. B: At. Mol. Opt. Phys.* **38** L357
- [27] Haber L H, Doughty B, and Leone S R *et al* 2009 *J. Phys. Chem. A* **113** 13152
- [28] Picard Y J *et al* 2014 *Phys. Rev. A* **89** 031401
- [29] Heuser S 2016 *et al Phys. Rev. A* **94** 063409
- [30] Loriot V *et al* 2017 *J. Opt.* **19** 114003
- [31] Cirelli C *et al* 2018 *Nat Commun* **9** 955
- [32] Busto D *et al* 2019 *Phys. Rev. Lett.* **123** 133201
- [33] Fuchs J *et al* 2020 *Optica* **7** 154
- [34] Bray A W, Naseem F and Kheifets A S 2018 *Phys. Rev. A* **97** 063404
- [35] Toma E S and Muller H G 2002 *J. Phys. B: At. Mol. Opt. Phys.* **35** 3435
- [36] Hockett P 2017 *J. Phys. B: At. Mol. Opt. Phys.* **50** 154002
- [37] Mauritsson J *et al* 2005 *Phys. Rev. A* **72** 013401
- [38] Jiménez-Galán Á, Argenti L and Martín F 2014 *Phys. Rev. Lett.* **113** 263001
- [39] Ivanov I A and Kheifets A S 2017 *Phys. Rev. A* **96** 013408
- [40] Maquet A and Taïeb R 2007 *J. Mod. Opt.* **54** 1847
- [41] Amusia M Ya, Cherepkov N A and Chernysheva L V 1972 *Phys. Lett. A* **40** 15
- [42] Kheifets A S 2013 *Phys. Rev. A* **87** 063404
- [43] Dahlström J M and Lindroth E 2014 *J. Phys. B: At. Mol. Opt. Phys.* **47** 124012; Corrigendum: Dahlström J M and Lindroth E 2016 *J. Phys. B: At. Mol. Opt. Phys.* **49** 209501
- [44] Vinbladh J, Dahlström J M and Lindroth E 2019 *Phys. Rev. A* **100** 043424

- [45] Carette T, Dahlström J M, Argenti L and Lindroth E *et al* 2013 *Phys. Rev. A* **87** 023420
- [46] Lysaght M A, van der Hart H W and Burke P G 2009 *Phys. Rev. A* **79** 053411
- [47] Hutchinson S, Lysaght M A and van der Hart H W 2013 *Phys. Rev. A* **88** 023424
- [48] Lambropoulos P 1976 *Advances in Atomic and Molecular Physics* **12** 87
- [49] Laurent G *et al* 2012 *Phys. Rev. Lett.* **109** 083001
- [50] Ullrich J *et al* 2003 *Rep. Prog. Phys.* **66** 1463
- [51] Madden R P, Ederer D L and Codling K 1969 *Phys. Rev.* **177** 136
- [52] Dehmer J L 1978 *Le Journal de Physique Colloques* **39** C4-42
- [53] Kennedy D J and Manson S T 1972 *Phys. Rev. A* **5** 227
- [54] Houlgate R G, Codling K, Marr G V and West J B 1974 *J. Phys. B: At., Mol. Phys* **7** L470
- [55] Codling K, Houlgate R G, West J B and Woodruff P R 1976 *J. Phys. B: At., Mol. Phys.* **9** L83
- [56] Reid K L 2003 *Annu. Rev. Phys. Chem.* **54** 397
- [57] Reid K L 2012 *Molecular Physics* **110** 131
- [58] Gisselbrecht M *et al* 2005 *Rev. Sci. Instrum.* **76** 013105
- [59] Guyétand O *et al* 2008 *J. Phys. B: At., Mol. Opt. Phys* **41** 065601
- [60] Lebech M, Houver J C and Doweck D 2002 *Rev. Sci. Instrum.* **73** 1866
- [61] Veyrinas K *et al* 2016 *Faraday Discuss.* **194** 161
- [62] Veyrinas K *et al* 2013 *Phys. Rev. A* **88** 063411
- [63] Born M and Wolf E 1980 *Principles of Optics* (Pergamon, New York)
- [64] Southworth S H *et al* 1986 *Nucl. Instr. Meth. Phys. Res. A* **246** 782
- [65] Becker U 1998 *J Electron Spectrosc. Relat. Phenom.* **96** 105–15
- [66] Mondal S *et al* 2014 *Phys. Rev. A* **89** 013415
- [67] Fano, U 1985 *Phys. Rev. A* **32** 617
- [68] Starace A F 1970 *Phys. Rev. A* **2** 118
- [69] Düsterer S *et al* 2016 *J. Phys. B: At. Mol. Opt. Phys.* **49** 165003
- [70] Meyer M *et al* 2008 *Phys. Rev. Lett.* **101** 193002
- [71] Hockett P *et al* 2014 *Phys. Rev. Lett.* **112** 223001
- [72] Baykusheva D and Wörner H J 2017 *J.Chem. Phys.* **146** 124306
- [73] Hockett P, Frumker E, Villeneuve D M and Corkum P B 2016 *J. Phys. B: At. Mol. Opt. Phys.* **49** 095602
- [74] Cattaneo L *et al* 2018 *Nature Phys* **14** 733
- [75] Lucchese R R *et al* 2002 *Phys. Rev. A* **65** 020702
- [76] Doweck D and Lucchese R R 2012 *Dynamical Processes in Atomic and Molecular Physics* **39** 5